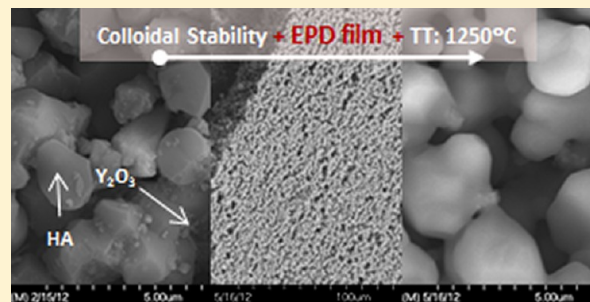


# Functionalizing Ti-Surfaces through the EPD of Hydroxyapatite/ NanoY<sub>2</sub>O<sub>3</sub>

P. Parente, A. J. Sanchez-Herencia, M. J. Mesa-Galan, and B. Ferrari\*

Instituto de Cerámica y Vidrio, CSIC, c/Kelsen 5, 28049 Madrid, Spain

**ABSTRACT:** Ceramic materials for skeletal repair and reconstruction are expanding to a number of different applications. Present research is addressing new compositions and performances to promote osseointegration through metal coatings. Nanotechnology plays a key role in this research because nanostructures can be introduced into implants to functionalize them and/or to enhance their properties, such as the thermal or mechanical response. In this work, the insertion of Y<sub>2</sub>O<sub>3</sub> nanoparticles into a hydroxyapatite (HA) coating of Ti using colloidal processing technology was developed. The suspensions of HA and Y<sub>2</sub>O<sub>3</sub> nanoparticles were formulated with a focus on zeta potential, particle size distribution, and viscosity for the codeposition of both phases by electrophoresis. The microstructure of the nanocomposite coating was optimized by adjusting the main parameters of the electrophoretic deposition process. A threshold value of the applied electric field for the composite shaping was identified. The results demonstrate that the Y<sub>2</sub>O<sub>3</sub> nanoparticles are homogeneously distributed in the coating and decrease in concentration as the distance from the substrate increases. As a consequence of the presence of the Y<sub>2</sub>O<sub>3</sub>, delays in the HA thermal decomposition and the improvement of metal–ceramic joining were observed.



## INTRODUCTION

Surface properties of a surgical implant play a significant role in the performance of orthopedic devices. In fact, events leading to osseointegration depend on the surface chemistry, topography, and roughness of the implant,<sup>1</sup> and usually, the classification of biomaterials is based on their interaction with the surrounding tissue.<sup>2</sup> Materials defined as biotolerant are largely accepted for implant manufacturing even though their biocompatibility is limited with regard to the response induced in the host by the material and degradation in the body environment. Among these, there are metallic materials currently used for surgical implants that possess good mechanical properties suitable for structural applications but have poor wear resistance; additionally, a mismatch often occurs between the nonphysiologic surface and the living tissue when these materials are used.<sup>3</sup> Surface modification and functionalization are proposed to address these problems and improve the performance of metal orthopedic devices. For this reason, several processing methods have been developed to provide the surface with microstructural design features that improve the durability and reliability of the metallic implants while promoting bone-tissue integration. Some of the microstructural designs include the development of porous surfaces, coating with special alloy particles, ceramics or hydroxyapatite (HA) or thermal treatment of the surfaces to reduce the grain size.<sup>2</sup> The appropriate use of organic or inorganic coatings on metallic surfaces makes bone formation possible at the interface between the implant surface and the surrounding tissue,<sup>3</sup> promoting osseointegration and improving implant integration.<sup>4</sup>

Particularly, inorganic bioactive coatings prevent some problems associated with the release of potentially harmful metal ions from the metallic substrate and increase the corrosion resistance of the implant.<sup>4</sup> HA is usually employed for this application because its chemical composition is similar to that of the mineral phase of natural bone.<sup>5,6</sup> Because of the inferior mechanical behavior of HA, efforts have been devoted to the development of composites, with a focus on improving the physical, mechanical, and biological properties of these materials. Recent studies have demonstrated that the addition of Y<sub>2</sub>O<sub>3</sub> to HA improves the mechanical behavior of the composite materials while maintaining good biocompatibility.<sup>7–9</sup> The incorporation of Y<sub>2</sub>O<sub>3</sub> dispersed into the HA favors the sintering process and controls the decomposition mechanisms of HA into calcium phosphates,<sup>10</sup> which makes HA + Y<sub>2</sub>O<sub>3</sub> composites promising materials for orthopedic metallic implant coatings with improved mechanical and functional properties.

To deposit HA-based composite coatings on implant surfaces, various processing methods have been used,<sup>3,11</sup> among which electrophoretic deposition (EPD) is especially attractive for the deposition of HA and other biomedical products on metallic substrates.<sup>4,12,13</sup> This technique allows for the production of controllable, uniform coatings with well-controlled thicknesses between 0.1 and 100 µm,<sup>4</sup> which depend

**Special Issue:** Electrophoretic Deposition

**Received:** May 28, 2012

**Revised:** November 6, 2012

**Published:** November 9, 2012

on the particle size of the deposited powders.<sup>14</sup> Homogeneous coatings can be deposited by EPD onto substrates with complex shapes and even onto porous structures. An additional advantage of the EPD technique is that the process does not require expensive or complicated equipment.

The EPD technique is based on the motion of charged particles dispersed in a liquid suspension toward an electrode under an applied electric field.<sup>11</sup> EPD experiments are conducted in a cell that consists of a cathode and an anode immersed in a stable colloidal suspension, providing a homogeneous electric field.<sup>15</sup> Similarly to other colloidal processes, suspension homogeneity is one of the main requirements when dealing with the compaction of a composite by EPD. The electrophoretic mobility of the particles, the conductivity of the suspension, the deposition time, and the applied voltage are the controllable parameters for the process. In the case of composites, control of the formulation and rheology of the suspension is also mandatory. Suspension flux behavior must be determined to avoid phase segregation and simultaneously allow for the particle motion.<sup>16,17</sup> Solid content, suspension stability and particle size, distribution and shape are the properties that determine EPD viability when reproduction of the composition of the suspension and reliability of the film thickness and the microstructure are desirable.

Our study of applying HA + Y<sub>2</sub>O<sub>3</sub> composite coatings to stainless steel and Ti substrates focuses on the dispersion of the second Y<sub>2</sub>O<sub>3</sub> phase in an HA matrix. The EPD method was selected due to its unique capabilities. Although suspensions in organic solvents have been regularly used for the application of HA coatings by an EPD process, previous work with the aqueous colloidal processing of HA shows that stable dispersions can be achieved in water. The key steps in the preparation of the HA composite coatings are identified in this paper, and the most relevant scientific results concerning this process are identified.

## MATERIALS AND METHODS

Commercial Ca<sub>10</sub>(PO<sub>4</sub>)<sub>6</sub>OH<sub>2</sub> (Ca: P ratio of 1.67: 1, from Plasma-Biotol, U.K.) and Y<sub>2</sub>O<sub>3</sub> (99.995% TREO from Overlack, Germany) powders were used as the starting materials. Depending on the particle dimensions, the size distribution was measured with a laser analyzer (Mastersizer S, Malvern Instrument Ltd., U.K.) or dynamic light scattering (DLS, Zetasizer Nano ZS, Malvern Instruments Ltd., U.K.) for micrometre and nanometre sized powders, respectively. The specific surface areas (BET) of the HA and Y<sub>2</sub>O<sub>3</sub> determined by one point N<sub>2</sub> adsorption (monosorb, Quantachrome, U.S.A.) were 1.1 m<sup>2</sup>/g and 13 m<sup>2</sup>/g, respectively.

The zeta potentials for both of the pure starting powders were studied as a function of pH and dispersant content by microelectrophoresis (Zeta-Meter 3.0+, Zeta-Meter, Inc., U.S.A.) and laser doppler velocimetry (Zetasizer Nano ZS, Malvern Instruments Ltd., U.K.) for HA particles (micrometre) and Y<sub>2</sub>O<sub>3</sub> (nanometre), respectively. For these measurements, colloidal suspensions were prepared in 10<sup>-2</sup> M solutions of KCl, with powder concentrations ranging from 1 to 0.1 g/cm<sup>3</sup>. The concentration was optimized depending on the powder and the equipment employed. Polyacrylic acid (PAA, *M<sub>w</sub>* = 2000, Acros Organics, U.S.A.) was used as the anionic dispersant. To ensure the dissociation of the PAA when added to the powder, dilutions of the pure dispersant were prepared in an ammonia solution with a 1.5 molar ratio of PAA/NH<sub>3</sub>.

Hydrochloric acid (HCl) and tetramethylammonium hydroxide (TMAH) (Sigma Aldrich, Germany) were used to adjust the suspension pH of the concentrated slurries. Carboxymethyl cellulose (CMC, OPTAPIX PA4G, Zschimmer-Schwarz, Germany) was added as a binder. A suspension of HA with a dispersion of 10 wt % Y<sub>2</sub>O<sub>3</sub> (referred to as HA + Y<sub>2</sub>O<sub>3</sub>) was prepared by adding the starting powders to deionized water after the pH of the liquid was adjusted with tetramethylammonium hydroxide (TMAH, Sigma-Aldrich), and an optimized amount of PAA was added. Magnetic stirring was used to mix the suspension. Dispersion and homogenization were achieved by sonicating with a 400 W probe (Hielscher UP400S, Germany) for 120 s and milling (using alumina balls) for 4 h.<sup>16</sup>

Rheological measurements were carried out on the concentrated slurries with a double cone–plate insert using a Rheo Stress RS-50-rheometer (Haake, Karlsruhe, Germany), and sedimentation tests were performed in a 25 mL graduated cylinder with 10, 30, and 45 vol. % solid concentrations.

The EPD cell consisted of a 30 mL glass beaker containing the suspension. The working electrode (cathode) and the counter electrode (anode) were placed at a distance of 2 cm. AISI 304 stainless steel or Ti discs were employed as the working electrodes (prepared as described elsewhere<sup>18</sup>), whereas a graphite foil of similar dimensions was used as the counter electrode. Prior to use in the EPD cell, the working electrodes were degreased and cleaned following a standardized protocol. Electrophoretic deposition was performed under galvanostatic conditions at applied current densities of up to 1.5 mA/cm<sup>2</sup> and deposition times of up to 20 min with an AMEL power source (551, U.K.). An area of approximately 1.5 × 2 mm<sup>2</sup> was dipped in the suspension during the EPD process and then covered. The deposited area was dried under room conditions after the EPD process, and the mass variation of each sample was measured with an analytical balance.

Dynamic sintering tests were performed on green pieces with dimensions of 5 × 5 × 10 mm<sup>3</sup> and a relative density of 63% (related to the theoretic density calculated through the Rule of Mixtures). These pieces were ground from samples obtained by slip casting 30 vol. % HA + Y<sub>2</sub>O<sub>3</sub> suspensions in a porous mold. A push-rod dilatometer (Netzsch, Germany) was used. Heating and cooling rates of 5 °C/min, up to 1450 °C, were used.

The HA + Y<sub>2</sub>O<sub>3</sub> coatings were dried in air for 48 h prior to sintering at 1250 °C for 90 min with heating and cooling rates of 5 °C/min.<sup>10</sup> An alumina tubular furnace with a flowing Argon atmosphere (Severn Furnaces Limited, U.K.) was employed to sinter the coating to the metallic substrates. X-ray diffraction (XRD) analysis of the as-deposited and sintered coatings was performed using a Bruker D8 Advance diffractometer (Germany). The microstructure was investigated on the surface of the coating and fracture samples using a field emission scanning electron microscope (FE-SEM, Hitachi S-4700, Japan).

## RESULTS AND DISCUSSION

### Optimisation of the Powder Mixture in Suspension.

Figure 1 shows the evolution of the zeta potential of the HA and Y<sub>2</sub>O<sub>3</sub> particles as a function of the pH. The zeta potential of the HA under adverse chemical conditions, such as in strong acid media, was determined to fit the isoelectric point (IEP). HA presents an IEP in the acid range of 3.5 < pH < 4.5. The IEP of the Y<sub>2</sub>O<sub>3</sub> was accurately measured and corresponds to a pH of 7.1 ± 0.1. Similar zeta potential values for HA powders have been reported in the literature,<sup>19–21</sup> whereas the zeta

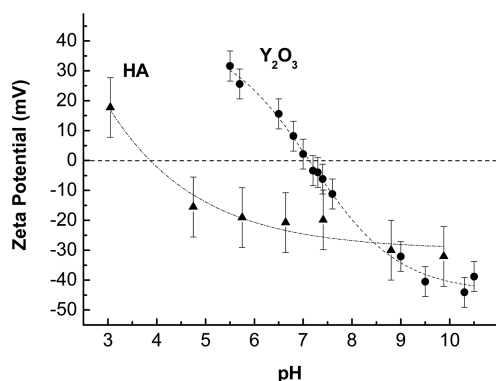


**Figure 1.** Zeta potential evolution of aqueous suspensions of the HA and  $Y_2O_3$  as a function of pH. Dotted lines have been provided as guides.

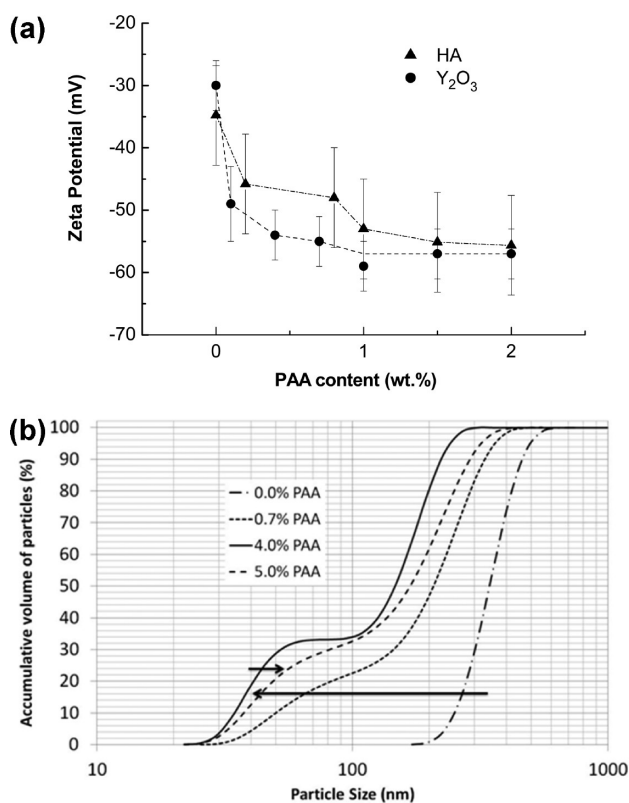


**Figure 2.** (a) Zeta potential evolution of aqueous suspensions of the HA and  $Y_2O_3$  as a function of PAA content. The dotted lines have been provided as guides. (b) Volumetric particle size distribution of the  $Y_2O_3$  nanoparticles as a function of the vol.% PAA addition.

potential evolution of the  $Y_2O_3$  is reported here for the first time. Although phosphate and calcium sites on the surface of the polycrystalline structure of the HA particles exhibit different charges depending on the pH, it is important to note that the zeta potential offers a balance of the surface charge. Consequently, the plotted values determine the sense as well as the rate of the particle movement during electrophoresis. In this case, both the HA and  $Y_2O_3$  particles are negatively charged for basic pH values. A working range between  $9 < \text{pH} < 10$  was selected. The absolute value of the surface charge ( $< 30 \text{ mV}$ ) is sufficiently high to consider the suspensions of both the powders chemically and electrochemically stable.

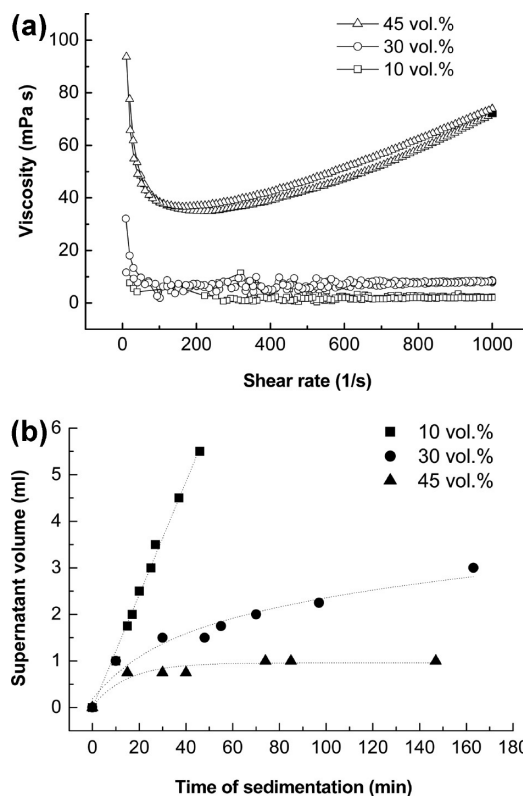


**Figure 3.** (a) Flow curves for the HAY suspensions with different solid contents. (b) Sedimentation rates of the HAY suspensions with different solid contents. Dotted lines have been provided as guides.

To provide the suspension with an additional electrosteric dispersion mechanism, PAA (up to 5 wt % on the basis of the solid content) was added to the monophasic suspensions that were prepared at a pH of 10. After the addition of the powder, the pH was readjusted to ensure the maximum deprotonation of the carbonyl group of the dispersant adsorbed on both the HA and  $Y_2O_3$  surfaces. The zeta potential variation with the dispersant addition (Figure 2a) shows the adsorption of the PAA chains through the increment of absolute values from  $\sim 30$  to  $50\text{--}60 \text{ mV}$ . This change in the zeta potential occurs quickly for 0.5 wt % PAA. Afterward, when 1.0 wt % PAA is achieved, further additions imply small changes in the zeta potential value, indicating that at this pH, the surface of both powders is saturated.<sup>22</sup>

These zeta potentials are expected for powders within the micrometer and submicrometer range (the average diameter of the HA is  $1.8 \mu\text{m}$ ). However the amount of dispersant required to completely stabilize the  $Y_2O_3$  nanoparticles could be higher due to its larger specific surface area. For that reason, the particle size distribution of the  $Y_2O_3$  nanopowder was determined for larger PAA concentrations. The results for the suspensions without PAA and with 0.7, 4.0, and 5.0 wt % PAA are plotted in figure 2b. The particle size distributions were determined for all of the PAA concentrations after ultrasound dispersion and stirring for 24 h. It can be clearly seen that the suspension prepared without PAA shows a monomodal particle size distribution in the micrometre range. Nanoparticle reagglomeration was observed after 24 h of stabilization time. The addition of 0.7 wt % PAA results in a bimodal population of particles, where the 20 vol. % is in the nanometre range. The nanometre volume fraction increases and achieves a maximum



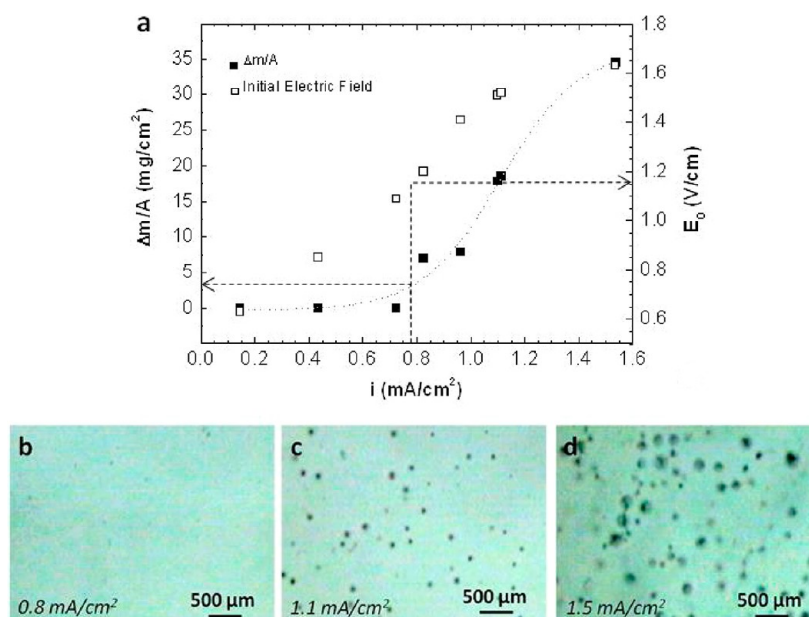


**Figure 4.** (a) Variation in mass per unit area as a function of the current density for an EPD time of 5 min: (■) mass per unit area and (□) initial electric field. The dotted lines have been provided as guides. Optical images show the coatings deposited at different current densities of (b) 0.8, (c) 1.1, and (d) 1.5 mA/cm<sup>2</sup> for 5 min.

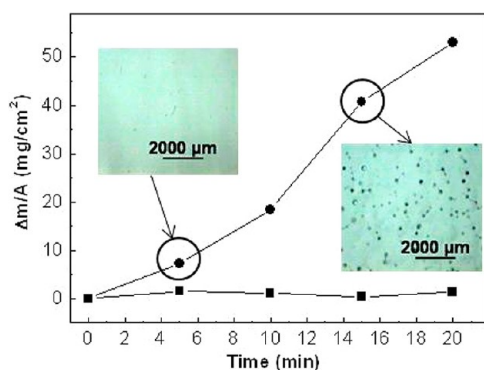


**Figure 5.** Variation in mass per unit area vs deposition time for  $i$ : 0.4 (■) and 0.8 (●) mA/cm<sup>2</sup>. Insets show optical micrographs of the HA + Y<sub>2</sub>O<sub>3</sub> coating surfaces for the assigned electric conditions.

when 4.0 wt.% PAA is added. A clear bimodal distribution with mean particle sizes centered in the 40–200 nm range can be observed. The addition of a larger amount of PAA (5 wt %) leads to a shift in the size distribution to micrometre values. This phenomenon can be attributed to the presence of free stabilizer in the liquid medium acting as a binder and surrounding particles.

The addition of 4.0 wt % PAA is the optimum condition to disperse the Y<sub>2</sub>O<sub>3</sub> nanoparticles. Because the radius of the nanoparticle is generally smaller than the Debye length when dispersion takes place in a polar medium such as water, the Smoluchowski approximation has been used to determine the zeta potential of the Y<sub>2</sub>O<sub>3</sub> nanoparticles. Hence, the electrophoretic mobility corresponding to a zeta potential of 50–60 mV in Y<sub>2</sub>O<sub>3</sub> suspensions is approximately  $4.5 \times 10^{-4}$  cm<sup>2</sup>/(V s). In the case of HA suspensions, 1 wt % PAA was considered to provide the particles with a similar mobility while limiting the concentration of free-stabilizer in the solution to the greatest extent possible.

Once the surface stability was guaranteed, high solid content slurries were prepared. The slurries were homogenized by

milling with alumina balls and adding CMC to improve compaction and preserve the uniformity of the layer with regard to shape and thickness. The CMC does not have a dispersing effect; rather, it affects the rheology by regulating the viscosity of the suspension.<sup>16</sup>

Due to the large size of the HA particles, the rheological behavior of the composed suspensions has received special attention. The viscosity and sedimentation rates of the slurries were measured to establish a suitable solid content. The suspension concentration should be low enough to allow for the movement of charged particles by electrophoresis toward the working electrode but high enough to ensure the homogeneous mixture of both particles during the entire duration of the EPD test. The flow curves and sedimentation rates of the HA + Y<sub>2</sub>O<sub>3</sub> suspensions with solid contents of 10, 30, and 45 vol. % are plotted in figures 3a,b, respectively. The suspension with the highest solid loading (45 vol. %) shows a shear thickening behavior that achieves viscosities higher than 40 mPa s. At these viscosity values, the movement of the particles toward the electrode could be disturbed. Conversely, the viscosity at the lowest solid loading (10 vol. %) is not sufficient to maintain the homogeneous suspension of the particles. Thus, HA particles sediment out, whereas the fine fraction of Y<sub>2</sub>O<sub>3</sub> floats in the supernatant, leading to powder segregation (see figure 3b). Finally, the suspension with a solid content of 30 vol. % was found to be adequate for coating purposes due to its near-Newtonian rheological behavior at viscosity values lower than 10 MPa s and its low sedimentation rate (see figure 3b). Both of these suspension characteristics ensure particle mobility by avoiding segregation and sedimentation during the EPD test.

**Shaping of Homogeneous HA + Y<sub>2</sub>O<sub>3</sub> Coatings on Stainless Steel by EPD.** The coatings created by the EPD process were investigated in terms of deposition efficiency and kinetics under different electrical conditions. Figure 4a represents the final mass gain per unit area ( $\Delta m/A$ ) as a function of the applied current density ( $i$ ) for EPD tests

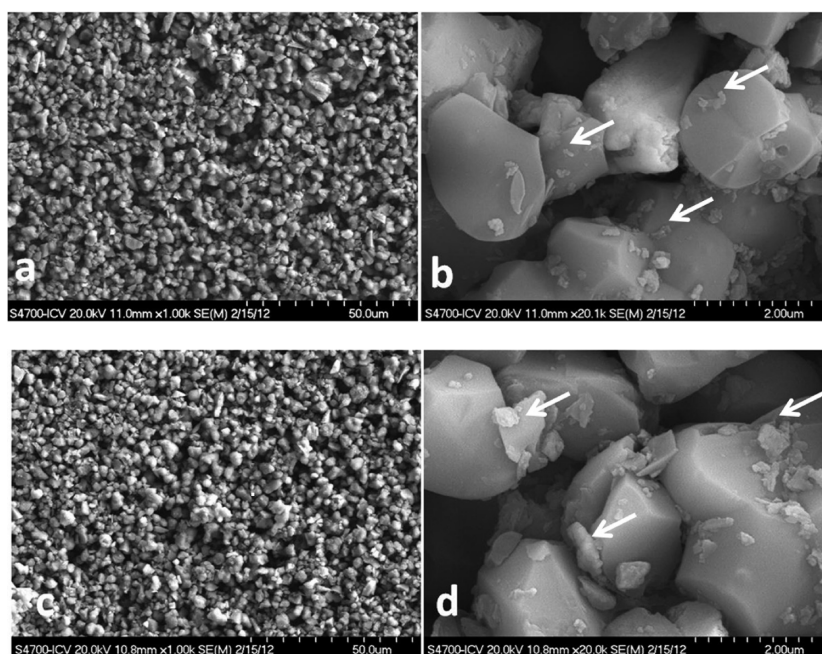


**Figure 6.** SEM images at different magnifications of the 7.35 and 34.49 mg/cm<sup>2</sup> coatings deposited by applying current densities of 0.8 (a and b) and 1.5 mA/cm<sup>2</sup> (c and d) for 5 min, respectively. Arrows indicate the Y<sub>2</sub>O<sub>3</sub> distribution.

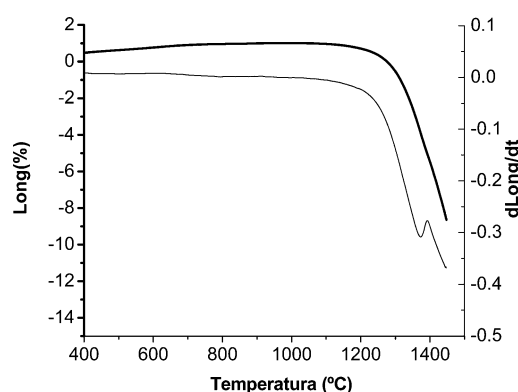


**Figure 7.** Dynamic sintering study of the HA + Y<sub>2</sub>O<sub>3</sub> bulk pieces.

performed for a constant time of 5 min. The initial electric field ( $E_0$ ) for each EPD test is also plotted. To demonstrate the effect of the applied electrical field on the coating homogeneity, optical micrographs of the surface of the coatings processed with current densities of 0.8, 1.1, and 1.5 mA/cm<sup>2</sup> for 5 min are included in Figure 4b–d. According to the data, the coatings correspond to a deposition of mass per unit area of 7.5, 18.5, and 34.5 mg/cm<sup>2</sup>, respectively. Porosity on the order of hundreds of micrometers (100–200 μm) is observed in the heaviest coatings (see Figure 4c,d). However, only in the coating created using a current density of 1.5 mA/cm<sup>2</sup> are cracks observed in the connecting paths between large pores. In contrast, the surfaces of the other two coatings appear homogeneous and crack-free, and the pores are randomly distributed.

The results plotted in Figure 4a show that deposition occurs when the applied current density is greater than 0.8 mA/cm<sup>2</sup>. From this point, deposition growth is relatively significant as the current density increases. According to the data collected for the initial electric field ( $E_0$ ), there is a threshold of 1.2 V/cm (noted in the plot) below which deposition does not occur.

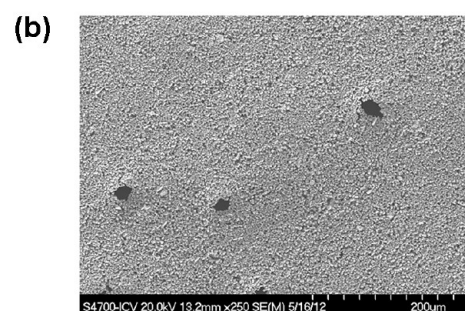
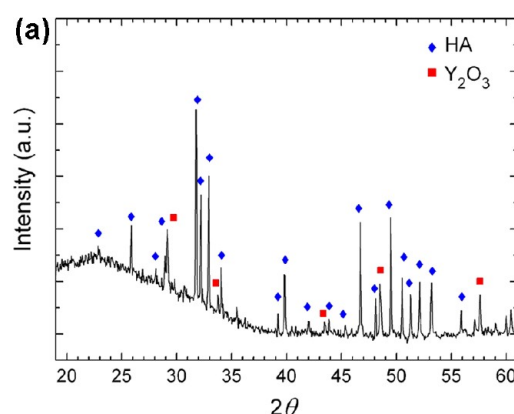


**Figure 8.** (a) XRD pattern of the HA + Y<sub>2</sub>O<sub>3</sub> sintered powder deposited on the Ti by EPD process and sintered at 1250 °C. (b) SEM micrograph of a general view of the surface of the sintered HA + Y<sub>2</sub>O<sub>3</sub> coating.

The test was designed such that the kinetics should force the system to be below  $E_0 < 1.2$  V/cm (for applied current densities of 0.4 mA/cm<sup>2</sup>) or immediately above  $E_0 \geq 1.2$  V/cm (for applied current densities of 0.8 mA/cm<sup>2</sup>). Figure 5 plots the mass gain per unit area versus the deposition times for two different sets of EPD experiments. Insets in this plot present optical micrographs of the surface of the HA + Y<sub>2</sub>O<sub>3</sub> coatings

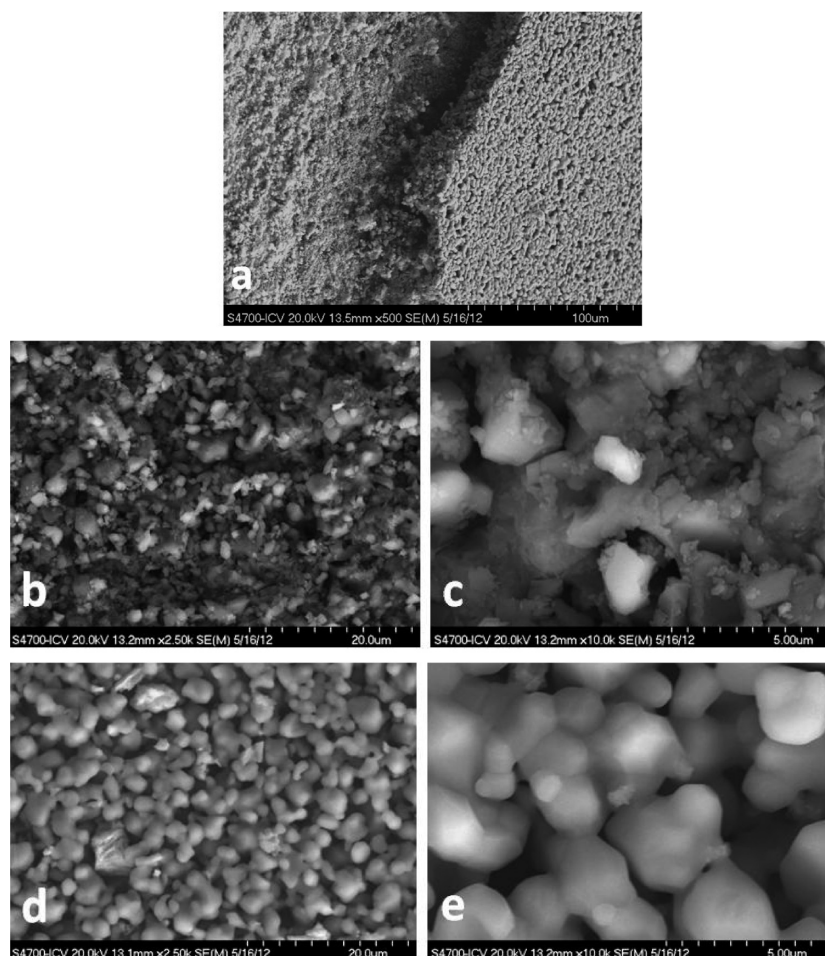


**Figure 9.** SEM images of a general view of the fresh fracture of a HA + Y<sub>2</sub>O<sub>3</sub> coating on Ti after sintering (a) and details at different magnifications of the first deposited layers (b and d) and the top surface (d and e) of the coating.

deposited using an applied current density of 0.8 mA/cm<sup>2</sup> for 5 and 15 min.

In Figure 5, the deposited mass per unit area increases linearly with the EPD time for samples coated with an applied current density of 0.8 mA/cm<sup>2</sup>, whereas no electrophoretic growth is observed with an applied current density of 0.4 mA/cm<sup>2</sup>. The kinetics for an applied current density of 0.8 mA/cm<sup>2</sup> shows uniform growth resulting in a homogeneous, highly cohesive, and well-adhered coating. Those layers present a certain porosity, which becomes more evident as the time allowed for deposition increases (a similar trend is observed with current density), with the size of the pores being on the order of hundreds of micrometers.

SEM micrographs of the surfaces of the coatings with large and small amounts of deposited mass are shown in Figure 6. Those micrographs correspond to the samples from the optical images that are shown in Figure 4b,d. Although there was a large difference in the deposited mass, the general views of the surfaces shown in Figure 6a,c demonstrates that the microstructures are similar. The images show a similar packing degree for both coatings. From respective details (see Figure 6b,d), it can be observed that the Y<sub>2</sub>O<sub>3</sub> nanoparticles are homogeneously distributed among the surrounding the HA particles. However, the fraction of Y<sub>2</sub>O<sub>3</sub> particles with  $D_{V50} = 40$  nm (Figure 2b) is significantly greater than the surrounding HA micrometre particles in the thinnest coating (Figure 6b), whereas the coarse Y<sub>2</sub>O<sub>3</sub> (particle fraction  $D_{V50} = 200$  nm in

figure 2b) is more evident in the coating obtained by applying a higher current density (Figure 6d).

The degree of packing, the amount and size of the porosity, and the homogeneous distribution of the nanoparticle fraction (Y<sub>2</sub>O<sub>3</sub>) around the HA are interconnected phenomena. It is well-known that a necessary but required condition for the EPD process is the preparation of a stable suspension. The packing and homogeneity of the microstructure are related to the deposition rate, which varies with the applied electric field and the particle mobilities.<sup>15,23–25</sup> In the past decade, EPD studies have focused on the determination of the deposition behavior of the particles when they arrive at the working electrode. The lack of comprehension and quantification of the phenomena related to the arrangement of the particles has motivated the description of phenomenological approaches.<sup>15,26–30</sup> Among the described mechanisms of arrangement and deposition, approaches based on particle flocculation are widely accepted. Flocculation occurs in the area surrounding the electrode due to several events, depending on the studied system. The described events are mainly related to the increase in particle concentration or the variation in the ionic strength by the accumulation and/or depletion of ions, which is ultimately due to the destabilization of the suspension. Faradaic and other simultaneous processes, such as gas bubbling, the electrohydrodynamics of the solvent and the charge exchange at the electrodes have a marked influence on suspension destabilization. These processes have been described in detail. However,



there are a few works that have correlated these phenomena with the adhesion of the particles or the way that the arrays formed close to the electrode at its surface. In this sense, four important points have been experimentally demonstrated and/or modeled: (i) preparation, electro-affinity and the charge distribution at the electrode surface have a relevant role in deposition;<sup>29</sup> (ii) the adhesion work decreases with the particle-substrate distance, promoting deposition;<sup>26</sup> (iii) the deposition growth depends on the magnitude of the difference between the particle size and the distance from the substrate where the suspension flocculation occurs;<sup>30</sup> and (iv) the electro-hydrodynamics of the solvent in combination with the previous enumerated factors can support deposition or completely preclude it.<sup>15,31</sup>

In our system, a remarkable threshold value has been detected for the applied electric field. Considering the smooth electrical conditions used in EPD tests, the existence of a threshold can be assigned to a lack of force, which can promote suspension flocculation. Above the electric field threshold, a lower current density causes a denser particle packing as the smaller particles can fill in the gaps between the larger ones.<sup>32</sup> Additionally, the lower current density results in less aggressive electrical conditions that prevent bubbling at the working electrode. The evidence for this becomes clear when comparing the optical micrographs in Figures 4 and 5. When the electric field increases, bubbling and a faster deposition rate prevent the deposited particles from rearranging which results in a relatively porous microstructure.

Furthermore, during compaction, two phenomena take place simultaneously. The first few particles that contact the substrate play a role in attracting other particles, and as the deposition kinetics increase due to the high local electric field, the subsequently deposited particles can prevent the formation of a continuous layer.<sup>26,32</sup> In this way, the gas bubbles nucleated on the surface of the anode between the particle arrays. If the arrays are well consolidated, this results in the formation of large pores cached within a dense skeleton, which results in a structure that is capable of remaining very stable during the sintering process.<sup>32,33</sup> However, those pores can exceed the size of the critical structural defect and promote cracking and the failure of the microstructure after sintering. Manipulation of the porosity in green compacts during the EPD process has been previously reported in the literature for other materials.<sup>27,34</sup>

**Sintered Coatings on Titanium Substrates.** Titanium and titanium alloys are the most commonly employed bioinert material for implants due to their good mechanical properties and biocompatibility. Bioactive ceramic coatings have been proposed as a means to improve the osteo-integration and durability of Ti-based implants. However, sintering of the ceramic layers deposited on full dense Ti usually promotes cracking due to the shrinkage of the coating during thermal processes. One of the strategies to solve this problem is to control the sintering behavior and design microstructures with residual porosity to reach the proper stresses and later promote bone growth onto the implants. Consequently, the shaping and consolidation of the porous coatings of HA + Y<sub>2</sub>O<sub>3</sub> onto the Ti substrates was proposed based on these processing parameters.

The results from the dynamic sintering study of the HA + Y<sub>2</sub>O<sub>3</sub> bulk pieces obtained by slip casting are plotted in figure 7. It is well-known that during a thermal treatment, HA can evolve into oxyhydroxyapatite (OHA) and oxyapatite (OH) and later decompose into calcium phosphates. It has been previously described<sup>10</sup> that the presence of well-dispersed Y<sub>2</sub>O<sub>3</sub> in the

microstructure can slow the HA decomposition due to the substitution of Y<sup>3+</sup> for Ca<sup>2+</sup> in the HA lattice. The dynamic study shows that the HA + Y<sub>2</sub>O<sub>3</sub> compact expands up to 1005 °C due to the in situ rehydration of the OHA and OH.<sup>10</sup> Later, after reaching a peak temperature of 1375 °C, the sample contracts, corresponding to a total shrinkage of 4%. This phenomenon is related to the final decomposition of HA in the calcium phosphates. Consequently, the initial temperature for shrinkage (1250 °C) has been considered for sintering HA + Y<sub>2</sub>O<sub>3</sub> coatings to avoid HA decomposition during the sintering step.

Based on these described results, the optimal processing conditions have been adjusted to shape the HA + Y<sub>2</sub>O<sub>3</sub> coatings on Ti substrates by an EPD process. Suspensions of 30 vol. % were prepared, and coatings were deposited under galvanostatic conditions at an initial electric field of 1.5 V/cm for 5 min. The coatings were then sintered at 1250 °C for 90 min in Ar atmosphere to avoid Ti oxidation. After sintering, a portion of the film was scratched, and powder was collected for analysis by XRD. Figure 8 shows the XRD spectrum of the sintered coating (see Figure 8a) and the SEM micrograph of the surface (see Figure 8b) with a focus on the well-defined macro-porosity caused by gas bubbling during the EPD process.

Characteristic diffraction peaks corresponding to both the HA and Y<sub>2</sub>O<sub>3</sub> powders can be observed in the XRD pattern of the sintered coating, confirming the presence of both deposited materials. The absence of other peaks, especially those characteristic of calcium phosphates, verifies the stability of the HA microstructure after the thermal treatment. The presence of Y<sub>2</sub>O<sub>3</sub> delays the reaction of the HA decomposition.

Additionally, the micrograph in Figure 8b demonstrates that the macro-porosity does not exceed the critical defect size for the HA + Y<sub>2</sub>O<sub>3</sub> microstructure. These pores are then integrated within the microstructure, resulting in a well-consolidated macro-porous layer.

Finally, Figure 9 shows a general view of the scratched HA + Y<sub>2</sub>O<sub>3</sub> layer. Details at two different magnifications on the free-surfaces of both sides of the fracture (Figure 9b–e) are also shown. The micrographs in Figure 9b,d are representative views of two levels and/or layers of the coating. The joining of the HA + Y<sub>2</sub>O<sub>3</sub> and Ti can be evaluated in Figure 9b,c, whereas a representative view of the top surface of the whole coating can be seen in Figure 9d,e. The micrograph in Figure 9a shows the uniformity of the HA + Y<sub>2</sub>O<sub>3</sub> coating and the homogeneity of its thickness. The micrographs in Figure 9b,d show the presence of a large amount of porosity in the range of 2–5 μm. However, the microstructures of the two levels/layers of the coating are extremely different. The first deposited layers contain an Y<sub>2</sub>O<sub>3</sub> enriched microstructure that is well joined to the Ti surface (a detail of the microstructure is shown in Figure 9c). The formation of necks between the HA particles, as well as the integration and localization of the nanoparticle fraction of the Y<sub>2</sub>O<sub>3</sub> at the triple points of the microstructure, are remarkable phenomena viewed on the surface of the HA + Y<sub>2</sub>O<sub>3</sub> coating (a detail of the microstructure is shown in Figure 9e).

The results of the sintering process show a dissimilar deposition of the HA microparticles and the Y<sub>2</sub>O<sub>3</sub> nanoparticles. The presence of large amounts of the nanophase in the first layers of the coating is beneficial for joining at the low temperatures used for sintering. Even when the formulation of the suspension has been adjusted to provide a similar surface charge for both particles, the mobility of the nanoparticles is

larger than that of the HA microparticles. In fact, the green coatings in Figure 6b,d show a preferential deposition of the fine over the coarse  $Y_2O_3$  nanofraction for short deposition times.<sup>35,36</sup> This provides evidence of the elevated lability and sensitivity of nanoparticles during the electrophoretic process.

## CONCLUSIONS

Titanium substrates were functionalized by the electrophoretic deposition of good-quality HA +  $Y_2O_3$  coatings that were uniform in thickness. A sintered porous HA +  $Y_2O_3$  microstructure with a dense skeleton joined to the Ti surface was fabricated using an aqueous EPD process. The insertion of a well-dispersed amount of  $Y_2O_3$  nanoparticles into the HA matrix was demonstrated. Pores were observed in the ranges of 2–5  $\mu m$  from the thermal treatment and hundreds of micrometers (100–200  $\mu m$ ) as consequence of water electrolysis trapping gas in the well-consolidated structure. The lability of the  $Y_2O_3$  nanoparticles resulted in a graded composition, where the amount of  $Y_2O_3$  was larger in the first micrometres of the layer and decreased toward the outer surface of the coating. The dispersed  $Y_2O_3$  phase slowed the HA decomposition and improved coating-Ti joining. Involvement of the  $Y_2O_3$  nanoparticles in the adherence of the coating to the substrate, further beneficial effects in the mechanical and functional performance of HA and the challenges associated with biotolerant coating fabrication all require more, detailed study.

Regarding the coating process, the IEP of the  $Y_2O_3$  was accurately determined to be a pH of  $7.1 \pm 0.1$ . A viscosity of 10 MPa s was found to be sufficient to avoid segregation without impeding the mobility of both particles. An electric field threshold of 1.2 V/cm was found to promote coating growth. This threshold was related to the force needed to promote the particle flocculation within the electrode surroundings.

## AUTHOR INFORMATION

### Corresponding Author

\*Phone: +34 917355840. Fax: +37 917355840. E-mail: bferrari@icv.csic.es.

### Notes

The authors declare no competing financial interest.

## ACKNOWLEDGMENTS

This work has been supported by the Spanish Ministry of Economy and Competitiveness (MINECO) under contracts MAT2009-14448-C02-01, MAT2012 38650-C02-02, and IPT-310000-2010-12.

## REFERENCES

- (1) Zingera, O.; Anselme, K.; Denzer, A.; Habersetzer, P.; Wieland, M.; Jeanfils, J.; Hardouin, P.; Landolt, D. *Biomaterials* **2004**, *25* (14), 2695–2711.
- (2) Geetha, M.; Singh, A. K.; Asokamani, R.; Gogia, A. K. *Prog. Mater. Sci.* **2009**, *54* (3), 397–425.
- (3) Nijhuis, A. W. G.; Leeuwenburgh, S. C. G.; Jansen, J. A. *Macromol. Biosci.* **2010**, *10* (11), 1316–1329.
- (4) Boccaccini, A. R.; Keim, S.; Ma, R.; Li, Y.; Zhitomirsky, I. J. *R. Soc. Interface* **2010**, *7*, S581–S613.
- (5) Barralet, J.; Best, S.; Bonfield, W. J. *Biomed. Mater. Res.* **1998**, *41* (1), 79–86.
- (6) Suchanek, W.; Yoshimura, M. J. *Mater. Res.* **1998**, *13* (1), 94–117.
- (7) Al-Haidary, J.; Al-Haidari, M.; Qrunfuleh, S. *Biomed. Mater.* **2008**, *3* (1), 015005.
- (8) Gunduz, O.; Daglilar, S.; Salman, S.; Ekren, N.; Agathopoulos, S.; Oktar, F. N. J. *Composite Mater.* **2008**, *42* (13), 1281–1287.
- (9) Auger, M. A.; Savoini, B.; Munoz, A.; Leguey, T.; Monge, M. A.; Pareja, R.; Victoria, J. *Ceram. Int.* **2009**, *35* (6), 2373–2380.
- (10) Parente, P.; Savoini, B.; Ferrari, B.; Monge, M. A.; Pareja, R.; Sanchez-Herencia, A. J. *Mater. Sci. Eng. C* <http://dx.doi.org/10.1016/j.msec.2012.11.013>.
- (11) Javidi, M.; Javadpour, S.; Bahrololoom, M. E.; Ma, J. *Mater. Sci. Eng. C* **2008**, *28* (8), 1509–1515.
- (12) Pishbin, F.; Simchi, A.; Ryan, M. P.; Boccaccini, A. R. *Surf. Coat. Technol.* **2011**, *205* (23–24), S260–S268.
- (13) Javidi, M.; Bahrololoom, M. E.; Javadpour, S.; Ma, J. *Mater. Corrosion-Werkstoffe Und Korrosion* **2009**, *60* (5), 336–343.
- (14) Boccaccini, A. R.; Roether, J. A.; Thomas, B. J. C.; Shaffer, M. S. P.; Chavez, E.; Stoll, E.; Minay, E. J. *J. Ceram. Soc. Jpn.* **2006**, *114* (1325), 1–14.
- (15) Sarkar, P.; Nicholson, P. S. *J. Am. Ceram. Soc.* **1996**, *79* (8), 1987–2002.
- (16) Gonzalo-Juan, I.; Ferrari, B.; Colomer, M. T.; Sanchez-Herencia, A. J. *J. Membr. Sci.* **2010**, *352* (1–2), 55–62.
- (17) Garcia, P.; Ferrari, B.; Moreno, R.; Sanchez-Herencia, A. J.; Colomer, M. T. *J. Eur. Ceram. Soc.* **2007**, *27* (13–15), 4241–4244.
- (18) Neves, R. G.; Escribano, J. A.; Ferrari, B.; Gordo, E.; Sanchez-Herencia, J. A. *Key Eng. Mater.* **2012**, *520*, 335–340.
- (19) Uskokovic, V.; Odsinada, R.; Djordjevic, S.; Habelitz, S. *Arch. Oral Biol.* **2011**, *56* (6), 521–532.
- (20) Kandori, K.; Kuroda, T.; Togashi, S.; Katayama, E. *J. Phys. Chem. B* **2011**, *115* (4), 653–659.
- (21) Kandori, K.; Toshima, S.; Wakamura, M.; Fukusumi, M.; Morisada, Y. *J. Phys. Chem. B* **2010**, *114* (7), 2399–2404.
- (22) Helgeson, M. E.; Hodgdon, T. K.; Kaler, E. W.; Wagner, N. J.; Vethamuthu, M.; Ananthapadmanabhan, K. P. *Langmuir* **2010**, *26* (11), 8049–8060.
- (23) Ferrari, B.; Moreno, R. J. *Eur. Ceram. Soc.* **2010**, *30* (5), 1069–1078.
- (24) Ferrari, B.; Santacruz, I.; Nieto, M. I.; Moreno, R. J. *Eur. Ceram. Soc.* **2004**, *24* (10–11), 3073–3080.
- (25) Ji, C. Z.; Lan, W. H.; Xiao, P. J. *Am. Ceram. Soc.* **2008**, *91* (4), 1102–1109.
- (26) Kershner, R. J.; Bullard, J. W.; Cima, M. J. *J. Colloid Interface Sci.* **2004**, *278* (1), 146–154.
- (27) Besra, L.; Uchikoshi, T.; Suzuki, T. S.; Sakka, Y. *J. Am. Ceram. Soc.* **2008**, *91* (10), 3154–3159.
- (28) Van Tassel, J. J.; Randall, C. A. *J. Phys. Chem. C* **2007**, *111* (8), 3358–3365.
- (29) Riahifar, R.; Marzbanrad, E.; Dehkordi, B. R.; Zamani, C. *Mater. Lett.* **2010**, *64* (5), 559–561.
- (30) Radice, S.; Bradbury, C. R.; Mischler, S. J. *Eur. Ceram. Soc.* **2010**, *30* (5), 1079–1088.
- (31) Ristenpart, W. D.; Aksay, I. A.; Saville, D. A. *Phys. Rev. E* **2004**, *69* (2), 021405-1–021405-8.
- (32) Ma, J.; Wang, C.; Peng, K. W. *Biomaterials* **2003**, *24* (20), 3505–3510.
- (33) Kingery, W. D.; Francois, B. In *Interactions between grain boundaries and pores. Sintering and related phenomena*; Kuczynski, G. C., Hooton, N. A., Gibbon, C. F., Eds.; Gordon and Breach Science Publishers: New York, 1967; pp 471–498.
- (34) Moritz, K.; Moritz, T. J. *Eur. Ceram. Soc.* **2010**, *30* (5), 1203–1209.
- (35) Verde, M.; Caballero, A. C.; Iglesias, Y.; Villegas, M.; Ferrari, B. *J. Electrochem. Soc.* **2010**, *157* (1), H55–H59.
- (36) Verde, M.; Peiteado, M.; Caballero, A. C.; Villegas, M.; Ferrari, B. *J. Colloid Interface Sci.* **2012**, *373*, 27–33.